Unitary qubit lattice simulations of complex vortex structures



2012 Comput. Sci. Disc. 5 014013

(http://iopscience.iop.org/1749-4699/5/1/014013)

COMPUTATIONAL SCIENCE&DISCOVERY

# Unitary qubit lattice simulations of complex vortex structures

**George Vahala[1], Jeffrey Yepez[2], Linda Vahala[3] and Min Soe[4]**

[1] Department of Physics, William and Mary Williamsburg , VA 23185, USA
[2] Air Force Research Laboratory, Air Force Maui Optical and Supercomputing Site, Kihei, HI 96753, USA
[3] Department of Electrical and Computer Engineering, Old Dominion University, Norfolk, VA 23529, USA
[4] Department of Mathematics and Physical Sciences, Rogers State University, Claremore, OK 74017, USA

Received 11 February 2012, in final form 13 July 2012
Published 30 August 2012
*Computational Science & Discovery* **5** (2012) 014013 (19pp)
doi:10.1088/1749-4699/5/1/014013

**Abstract.** A quantum vortex is a topological singularity with quantized circulation, unlike a classical vortex with its continuous circulation strength. Quantum turbulence, envisaged as strong tangle of quantum vortices, of a Bose–Einstein condensate is examined by developing a unitary qubit lattice algorithm for the solution of the Gross–Pitaevskii equation. Earlier, it was shown that a certain class of initial conditions had a very short Poincare recurrence time for this Hamiltonian system. Here it is shown quantitatively that increasing the internal energy of the initial state leads to a systematic degradation of this class of solutions. Coupled Bose–Einstein condensate systems are investigated for a Hopf link class of initial conditions in which a vortex ring core is threaded by a linear vortex core that then closes toroidal around the vortex ring. These states are known as skyrmions and play a role in particle physics, astrophysics and condensed matter physics.

**Contents**





1749-4699/12/014013+19$33.00

## 1. Introduction

Vortices are essential structures arising in fluid, plasma and quantum turbulence [1]. In classical physics, however, the vortex is a somewhat fuzzy concept partially recognized by the circulation around its vortex core. This fuzziness is a consequence of the fact that the circulation strength is a continuous variable with the vortices having continuously varying spatial extents. Classical vortices arise in incompressible flows as well as in compressible flows. On the other hand, the quantum vortex [2] is a topological singularity with the vortex core having zero mean superfluid density. Thus for quantum vortices to exist it is essential for one to deal with a compressible fluid. The circulation about a quantum core is quantized and a quantum core acts like a branch cut: there is a phase discontinuity as one circumnavigates the core. Moreover, it can be shown that vortices with higher winding numbers $n$ (i.e., with a phase discontinuity on circumnavigating the core) are energetically unfavorable so that in quantum turbulence one typically finishes with a tangle quantum vortices with a winding number of 1.

In this paper, we continue our studies of complex quantum vortex structures using our unitary qubit lattice algorithms [3–8]. The beauty of these mesoscopic representations is their extreme parallelizablity and low memory requirements [9]. This permits production runs on previously unattainable grids (e.g., we have performed production runs on quantum turbulence to grids $5760^3$ using just 12 000 cores [9, 10]). Of much interest, both experimentally and computationally, is the subject of quantum turbulence in Bose–Einstein condensates (BECs) [11–16]. For weakly interacting BEC gases, the ground state is given by the Gross–Pitaevskii (GP) equation [17] (an equation which arises also in nonlinear optics and plasma physics, where it is known as the nonlinear Schrodinger equation [18])—of Hamiltonian form. While all Hamiltonian systems with bounded phase space have a Poincare recurrence of initial conditions, nearly all continuous Hamiltonian systems exhibit a Poincare recurrence time that is essentially infinite [19, 20]. Earlier [21, 22], we found a class of initial conditions which exhibits a remarkably short Poincare recurrence time. Here we will perturb this class of initial conditions and observe the sensitivity of the extremely short Poincare time to certain parameters.

There are more complex quantum structures when one considers coupled BECs. In particular, we consider the evolution of an unstable skyrmion [23] under periodic boundary conditions. A skyrmion is topologically equivalent to two linked quantum vortices: the first BEC yielding a ring vortex core which is interlaced by the second BEC whose line vortex core threads the ring vortex core and then closes toroidally to reconnect the line core. In knot theory it is known as a Hopf link. We shall find that the initial skyrmion will evolve into a lattice of multiple small skyrmions.

There is much interest ([25, 26, 27] and references therein), maybe too much, in the quantum turbulence community in finding an interrelationship between quantum and classical turbulence, and in particular in the existence of the Kolmogorov energy spectrum for the classical regime. Several major difficulties arise in seeking this comparison: quantum turbulence essentially requires a compressible superfluid, and it is an oversimplification to assume that compressible effects disappear in the 'asymptotic' region of a quantum vortex. While this may be true if there is only a single quantum vortex in the system, it is very doubtful when many vortices are present and interacting with each other. Second, nonlocal effects play a critical role in quantum turbulence. We discuss some of the essential differences between a classical and quantum vortex in section 2, while in section 3 we consider the parameter regimes that yield remarkably short Poincare recurrence times and then perturb these parameters and see the consequent degradation of the very short Poincare recurrence. Coupled BECs and the evolution of a particular Hopf link (known as a skyrmion) are discussed in section 4. In the appendix, we briefly outline the unitary qubit algorithm and present some of the weak and strong scalings on various supercomputing platforms. The algorithm shows excellent parallelization to over 200 000 cores.

## 2. Quantum vortices

In *incompressible* classical fluid turbulence, one solves for the evolution of the velocity field $\mathbf{v}$ from the Navier–Stokes equation (under the assumption of constant density)

$$\nabla \cdot \mathbf{v} = 0, \quad \frac{\partial \mathbf{v}}{\partial t} + \mathbf{v} \cdot \nabla \mathbf{v} = -\nabla p + \nu \nabla^2 \mathbf{v}, \quad -\nabla^2 p = \nabla \cdot (\mathbf{v} \cdot \nabla \mathbf{v}) \,. \tag{1}$$

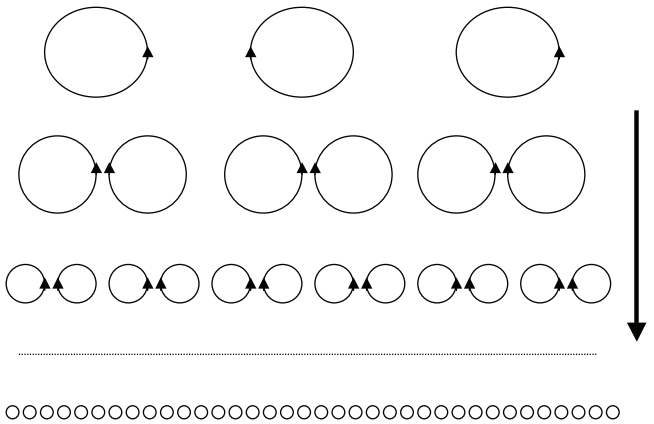

**Figure 1.** A cartoon of the Richardson energy cascade from large-scale to small-scale eddies in incompressible fluid turbulence. In actual turbulence, vortices of many different scales will co-exist. The density throughout the whole flow is constant: $\rho\,(\mathbf{x}, t) \equiv$ const.

The pressure field, because of incompressibility, is simply a bilinear functional of the velocity field and $\nu$ is the viscosity. Of much interest is the energy spectrum of classical incompressible homogeneous isotropic turbulence in three dimensions. The energy spectrum $E\,(k)$ is typically divided into three distinct wave number ranges: an input range, an inertial range and a dissipative range. For steady state turbulence, energy is fed into the incompressible fluid at large scales, creating large-scale eddies (i.e., vortices). The nonlinear interactions in the Navier–Stokes equation cascade this energy into smaller and smaller eddies until one reaches wave number scales at which the dissipative term in (1), $\nu k^2 \mathbf{v}\,(\mathbf{k}, t)$, dominates the nonlinear energy-conserving terms and so brings to an end the so-called Kolmogorov inertial range energy $k^{-5/3}$ cascade. This inertial energy cascade is shown in the cartoon of figure 1.

In actual turbulence, at any particular instant, there will be many different size vortices present in the flow and a mathematical definition of a classical vortex is fuzzy.

Turbulence has also been studied experimentally in superfluid helium with liquid $^4$He undergoing Bose–Einstein condensation (BEC) at sufficiently low temperatures [14, 15, 16, 27]. However, the recent success of BEC of weakly interacting gases has made possible a detailed study of quantum turbulence since the evolution of the ground state wave function of the BEC is well described by the GP equation [1]

$$\mathrm{i}\,\hbar \frac{\partial \varphi}{\partial t} = -\frac{\hbar^2}{2m}\nabla^2 \varphi + \left[g\,|\varphi|^2 - \mu\right]\varphi. \tag{2}$$

$\varphi$ is the one-particle wave function, $g$ is the nonlinear coupling parameter representing the s-wave scattering of the weak bosonic interactions under the mean field approximation and $\mu$ is the chemical potential. For numerical purposes, it is convenient to rescale the GP equation (2) into the form

$$\mathrm{i}\frac{\partial \varphi}{\partial t} = -\nabla^2 \varphi + a\left[g\,|\varphi|^2 - 1\right]\varphi, \tag{3}$$

where $a$ is a spatial rescaling parameter. The GP is a ubiquitous equation of physics—reoccurring also in the field of nonlinear optics and plasma physics as the nonlinear Schrodinger equation. Under the Madelung transformation [11]

$$\varphi\,(\mathbf{x}, t) = \sqrt{\rho\,(\mathbf{x}, t)}\exp\left[\mathrm{i}\theta\,(\mathbf{x}, t)\,/2\right], \quad \mathbf{v}\,(\mathbf{x}, t) = \nabla\theta\,(\mathbf{x}, t)\,, \tag{4}$$

one can rewrite the GP (1) into the closed set of fluid-like conservation equations for $\rho$, $\mathbf{v}$:

$$\begin{aligned} &\frac{\partial \rho}{\partial t} + \nabla\cdot(\rho\mathbf{v}) = 0, \\ &\rho\left(\frac{\partial \mathbf{v}}{\partial t} + \mathbf{v}\cdot\nabla\mathbf{v}\right) = -g\nabla\left(\rho^2\right) + 2\rho\nabla\left(\frac{\nabla^2\sqrt{\rho}}{\sqrt{\rho}}\right). \end{aligned} \tag{5}$$

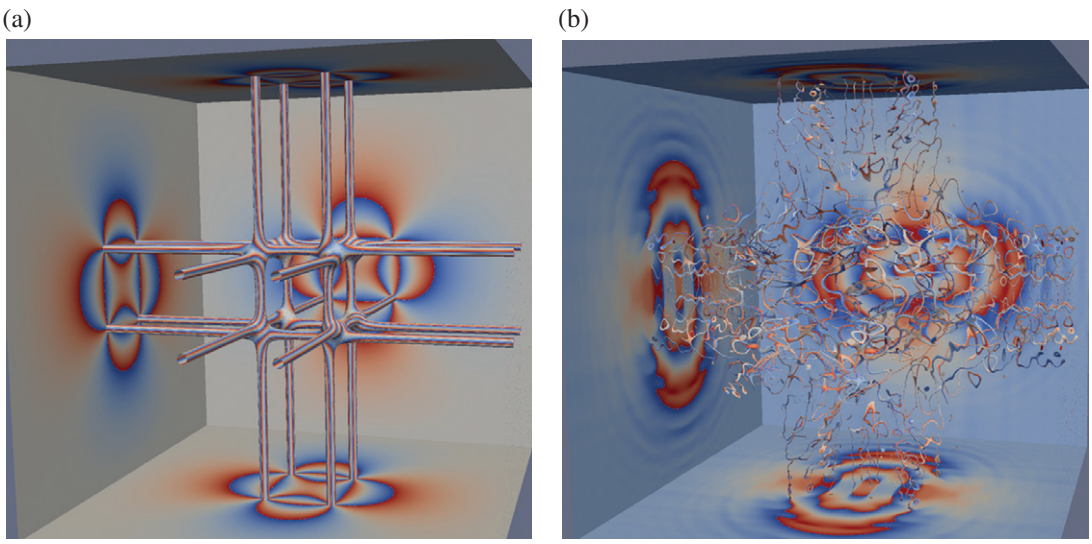


**Figure 2.** Density isosurfaces $|\varphi| / |\varphi|_{\max} = 1/16$ near the vortex core for 12 linear vortices with winding number 5: (a) $t = 0$ and (b) $t = 5000$. The phase information is shown on both the density isosurfaces and the walls: $\phi = 0$ (blue) and $\phi = 2\pi$ (red).

Thus we can identify $\rho$ as the superfluid density and $\mathbf{v}$ as the superfluid velocity. Moreover, $\varphi$ is the order parameter with a topological singularity at $\rho = 0$. This topological singularity gives rise to the quantum vortex core. The circulation about the vortex core is quantized, unlike the classical vortex circulation. Using Pade approximants [28], one can determine steady state linear vortex solutions to the GP (2): e.g., for winding number $n = 1$, using cylindrical polar coordinates

$$\varphi_0(r, \phi) = \mathrm{e}^{\mathrm{i}\phi} \left(\frac{1}{g}\right)^{1/2} \left(\frac{11ar^2(12 + ar^2)}{384 + ar^2(128 + 11ar^2)}\right)^{1/2}, \tag{6}$$

with $\varphi_0(0) = 0$, $|\varphi_0| \to g^{-1/2}$ as $r \to \infty$. Loosely speaking, the quantum vortex core acts as a branch point (figure 2) in the isosurface plots of $|\varphi_0(r)|$ for the vortex cores:

Here we consider 12 linear vortices (four in each plane) with winding number 5. If one examines the intersect of the linear vortex with the wall, one finds five branch cuts connecting each branch point (figure 2(a)). As this is energetically unstable, the initial condition is rapidly destroyed into loop vortices, tangled vortices as well as sound waves. Sound wave ripples are visible on the walls. The color coding on both the quantum vortex cores and the walls is $\phi = 0$ (blue) and $\phi = 2\pi$ (red). All the simulations are assuming periodic boundary conditions.

It is instructive to note the differences between the incompressible dissipative Navier–Stokes equation, (1), for classical turbulence over the compressible, conservative GP equation (5) for quantum turbulence. While the GP system (5) resembles a barotropic superfluid with 'classical' pressure $p \sim \rho^2$ there is also a novel nonlocal pressure, typically called the 'quantum' pressure, with its complex dependence on $\sqrt{\rho}$—the second term on the right-hand side of (5). It is this quantum pressure that permits quantum vortex reconnection [29, 30, 31, 32] without any dissipative terms in the evolution equation. On the other hand, classical vortex reconnection can only occur under dissipation. Because the GP equation is conservative, the total energy $E_{\mathrm{TOT}}(t) = \text{const}$. In the seminal work of Norec *et al* [11], this total energy can be decomposed into a kinetic energy $E_{\mathrm{kin}}(t)$, which includes both compressible and incompressible kinetic energies—a quantum energy $E_{\mathrm{qu}}(t)$ and an internal energy $E_{\mathrm{int}}(t)$:

$$E_{\mathrm{kin}}(t) = \int \mathrm{d}^3x \left[\sqrt{\rho}\mathbf{v}\right]^2, \quad E_{\mathrm{qu}}(t) = \frac{2}{a^2} \int \mathrm{d}^3x \left[\nabla\sqrt{\rho}\right]^2, \quad E_{\mathrm{int}}(t) = \frac{g}{a^2} \int \mathrm{d}^3x \, [\rho]^2. \tag{7}$$

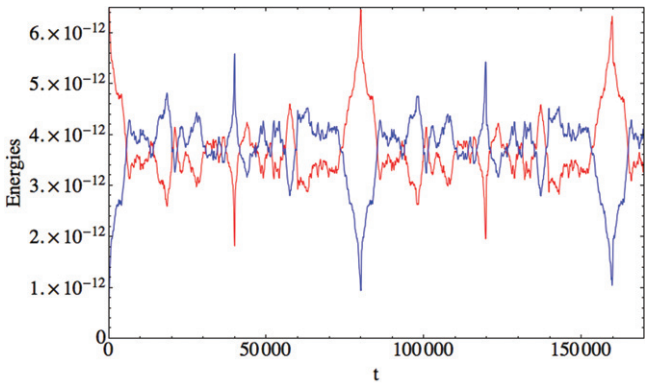


**Figure 3.** The time evolution of the kinetic energy (red) and the quantum energy (blue). The internal energy here is a factor of $10^{-6}$ smaller. There is semi-periodicity after 80 000 time steps with the extremal peaks decaying by only 2–4%. The qubit unitary algorithm conserves the total energy to within 0.5% of its initial value.

## 3. Poincare recurrence of initial conditions

Poincare proved that in every Hamiltonian system with bounded flows, the flow will pass arbitraril closely to the initial state after some appropriate time. This, of course, led to the famous dialog between Boltzmann (and his $H$-theorem) and Zermelo [33]. It is at the heart of the discussion between microscopic reversibility and kinetic irreversibility—between dynamics and statistical mechanics. Boltzmann's argument typically was that the recurrence time was basically so long as to be essentially infinite. However, we shall find, for the GP Hamiltonian system, that very short Poincare recurrence times can occur for parameter regimes

$$E_{\text{int}}(0) \ll E_{\text{kin}}(0), \quad E_{\text{qu}}(0). \tag{8}$$

We first consider the case of 12 linear vortices with winding number 1 and initial energies

$$E_{\text{int}}(0)/E_{\text{kin}}(0) = 2.6 \times 10^{-6}, \quad E_{\text{qu}}(0)/E_{\text{kin}}(0) = 0.095. \tag{9}$$

The time evolution of the energies $E_{\text{kin}}(t)$ and $E_{\text{qu}}(t)$ are shown in figure 3, with a very pronounced periodicity of 80 000 time steps. Actually, from the isosurface plots of $|\varphi|$ this is actually the half-period: the Poincare recurrence occurs every 160 000 time steps.

The corresponding vortex core isosurfaces are shown in figure 4; with phase information on the isosurfaces but now on the walls we present the wave function magnitudes $|\varphi|$: blue for $|\varphi| \to 0$ and red for $|\varphi| \to |\varphi|_{\max}$. There are four linear vortex cores intersecting each plane, giving the four a 'bulls eye'. These vortex cores then become unstable and oscillate, reconnect and break into vortex loops. This is readily seen in figure 4(b) at $t = 4600$. At the semi-Poincare recurrence time we again recover 12 linear vortices, but now their positions are plane inversions of their initial positions. The vortex cores are so thin that one cannot readily discern any phase information on these isosurfaces.

In figures 4(b) and (c), one sees a simple $2\pi$ phase discontinuity on circumnavigating the vortex cores, and in panel (d) one sees the residual effects of sound waves on the walls at the semi-Poincare recurrence time. One recovers the full Poincare recurrence of the initial conditions at $t = 179\,900$ along with sound waves.

When the initial internal energy is increased by a factor of $\sim 10^4$, one finds substantial effects on the evolution of the energies (figure 5(a)), with some clear degradation in the Poincare recurrence, $t = 179\,900$. On further increasing the internal energy, one sees the total loss of the very short Poincare recurrence (figure 5(b)).

The energy spectra dovetail with the isosurfaces of $|\varphi|$, as can be seen from figures 6(a)–(d). At $t = 0$, one has the 12 semi-isolated linear vortex cores. It can be shown that a single isolated quantum vortex core yields an *incompressible* kinetic energy spectrum

$$\text{isolated quantum vortex}: E_{\text{incomp}}(k) \sim k^{-3}, \quad E_{\text{comp}}(k) = 0, \tag{10}$$

with no compressible kinetic energy. However, in the case of our initial 12 linear vortices, there is a slight overlap of the asymptotic wave functions so that one now sees a very weak nonzero compressible energy

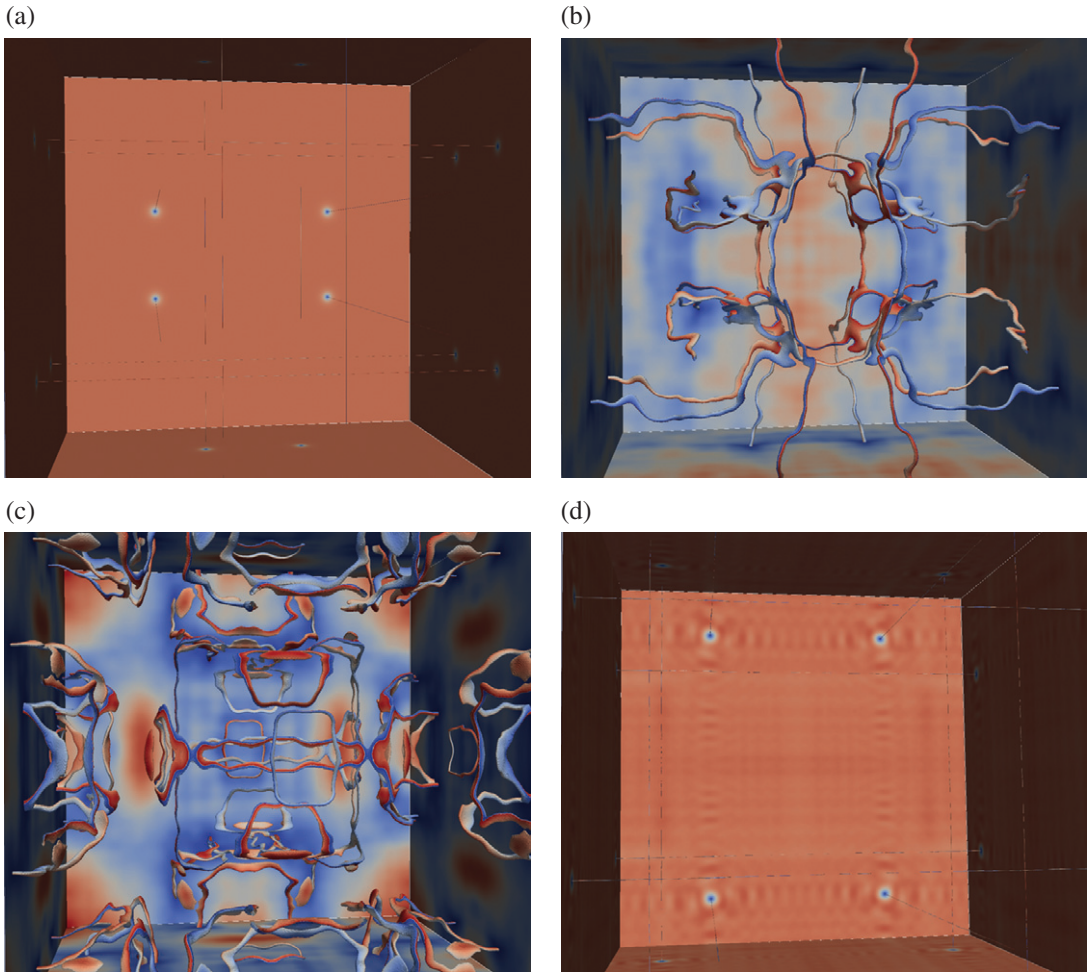


**Figure 4.** Isosurface plots of $|\varphi| / |\varphi|_{\max} = 1/64$ with phase information on the isosurfaces ($\phi = 0$ (blue) and $\phi = 2\pi$ (red)), while on the walls $|\phi|_{\text{walls}}$ values are plotted with a color scheme of blue (low) to red (high). (a) Initial 12 linear vortices, $t = 0$; (b) at $t = 4600$ after vortex reconnection has occurred; (c) at $t = 17\,400$ with multiple reconnections and vortex loop generations; (d) at $t = 79\,800$, which coincides with the extrema in the kinetic and quantum energies (figure 3) but which is actually the semi-Poincare recurrence time as the vortex cores are at a plane inversion symmetry of the initial state, $t = 0$. The full Poincare recurrence occurs at 179 800 and correlates with the kinetic and quantum energy extrema of figure 3. The grid $L^3 = 1000^3$.

spectrum (figure 6(a)). For $30 < k < 350$, at $t = 0$, both the incompressible kinetic energy and the quantum spectrum coincide and exhibit the $k^{-3}$ power law. At $t = 17\,500$, the spectra are as shown in figure 6(b) along with the $k^{-3.00}$ spectral line fit to the quantum energy for $75 \leqslant k \leqslant 300$—and for most times these are the typical spectral shapes although the magnitudes of the compressible and incompressible kinetic energies do fluctuate somewhat. While the incompressible kinetic energy exhibits a single power ($k^{-3}$) spectrum the compressible kinetic energy spectrum exhibits its usual three power law exponents [21]. Typically, but not always, the compressible kinetic energy spectrum is above the incompressible kinetic energy spectrum with the quantum energy spectrum being above both of them. The exceptional times in the spectral evolution occur either when the quantum vortices become minimal [21] and cannot sustain Kelvin waves (figure 6(c)) or near-integer multiples of the semi-Poincare recurrence time (figure 6(d)). For minimal vortex core isosurfaces the incompressible kinetic energy takes a very strong dip, while the compressible and quantum energy spectra become quite noisy (figure 6(c)). Around the multiples of the semi-Poincare recurrence time the compressible kinetic energy spectrum drops (figure 6(d)), reminiscent of its spectrum at $t = 0$, but now it has a significant

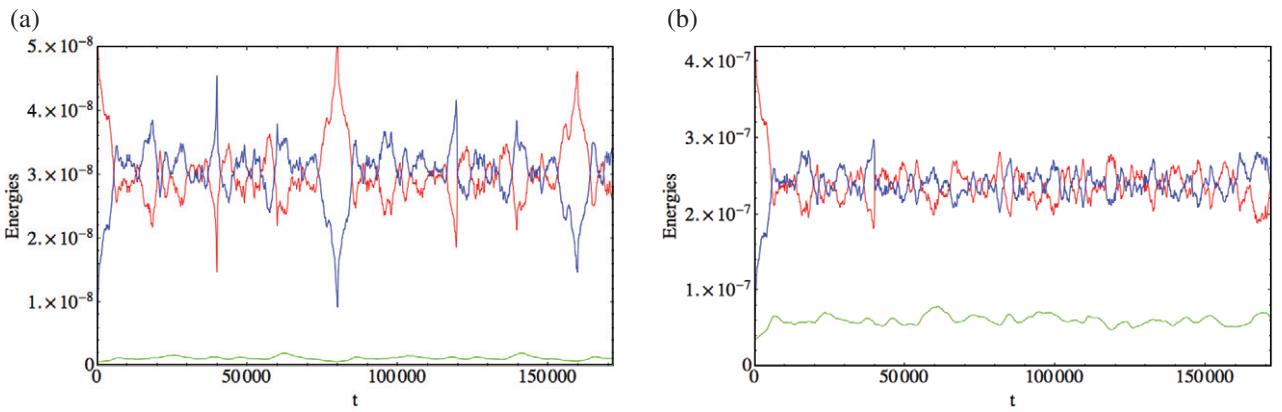


**Figure 5.** The time evolution of the kinetic energy (blue), the quantum energy (red) and the internal energy: (green) for increasing initial internal energy: (a) $E_{\rm int}(0)/E_{\rm kin}(0) = 1.1 \times 10^{-2}$, $E_{\rm qu}(0)/E_{\rm kin}(0) = 0.095$; (b) $E_{\rm int}(0)/E_{\rm kin}(0) = 7.5 \times 10^{-2}$, $E_{\rm qu}(0)/E_{\rm kin}(0) = 0.095$.

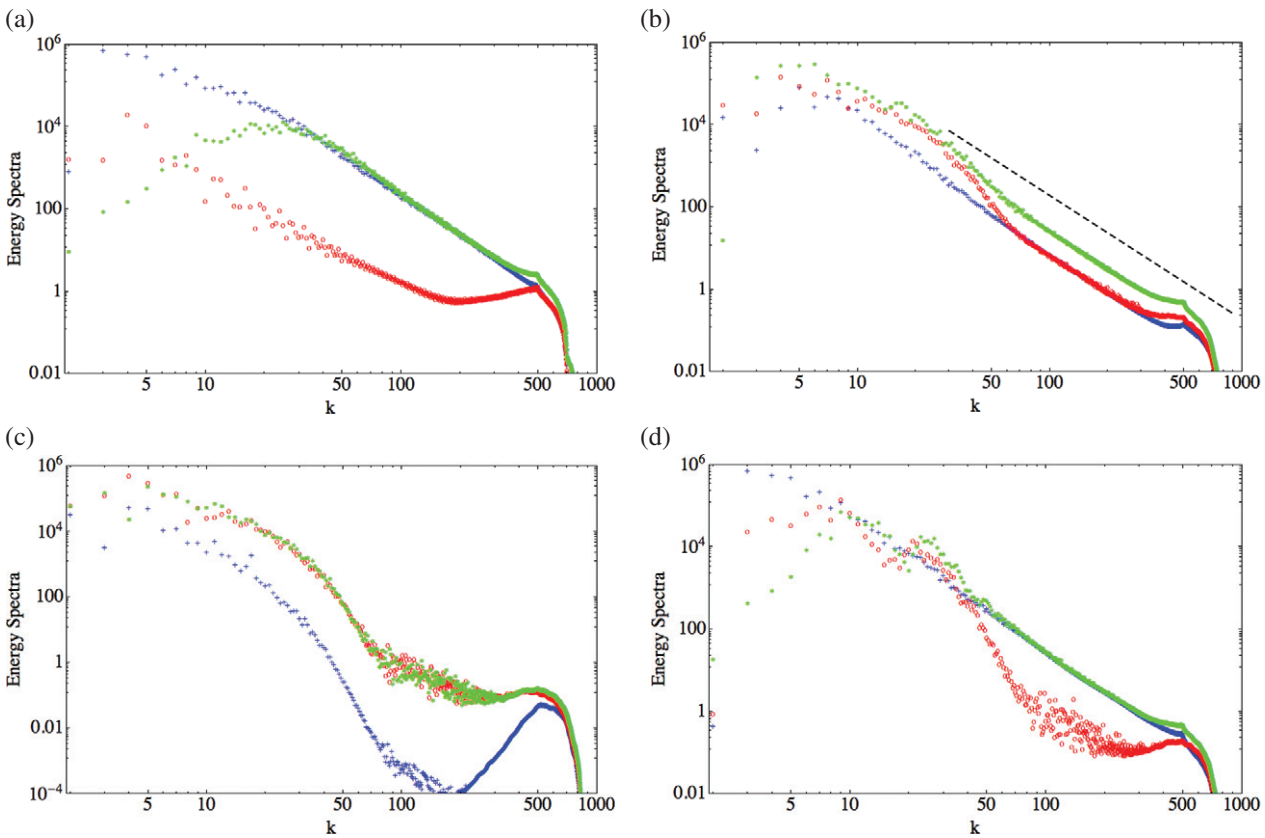


**Figure 6.** The spectra for incompressible kinetic energy (blue +), compressible kinetic energy (red o) and quantum energy (green $*$) for the case of negligible internal energy at (a) $t = 0$, (b) typical spectra, $t = 17\,500$, (c) vortex core minimization, $t = 57\,000$ and (d) semi-Poincare recurrence time, $t = 80\,000$. The grid $L^3 = 1000^3$. The dashed black curve in (b) is the $k^{-3}$ spectral line.

increase in spectral energy for small $k$, $5 \leqslant k \leqslant 50$. Persumably this may be attributable to the emission of sound waves which are absent at $t = 0$.

In the case of large internal energy (cf figure 5), the spectra for all times are similar to those in figure 6(b) (except, of course, at $t = 0$, which resembles that of figure 6(a)). In our spectral studies here, we are more concerned with spectral changes due to the loss of the very short Poincare recurrence time rather than with

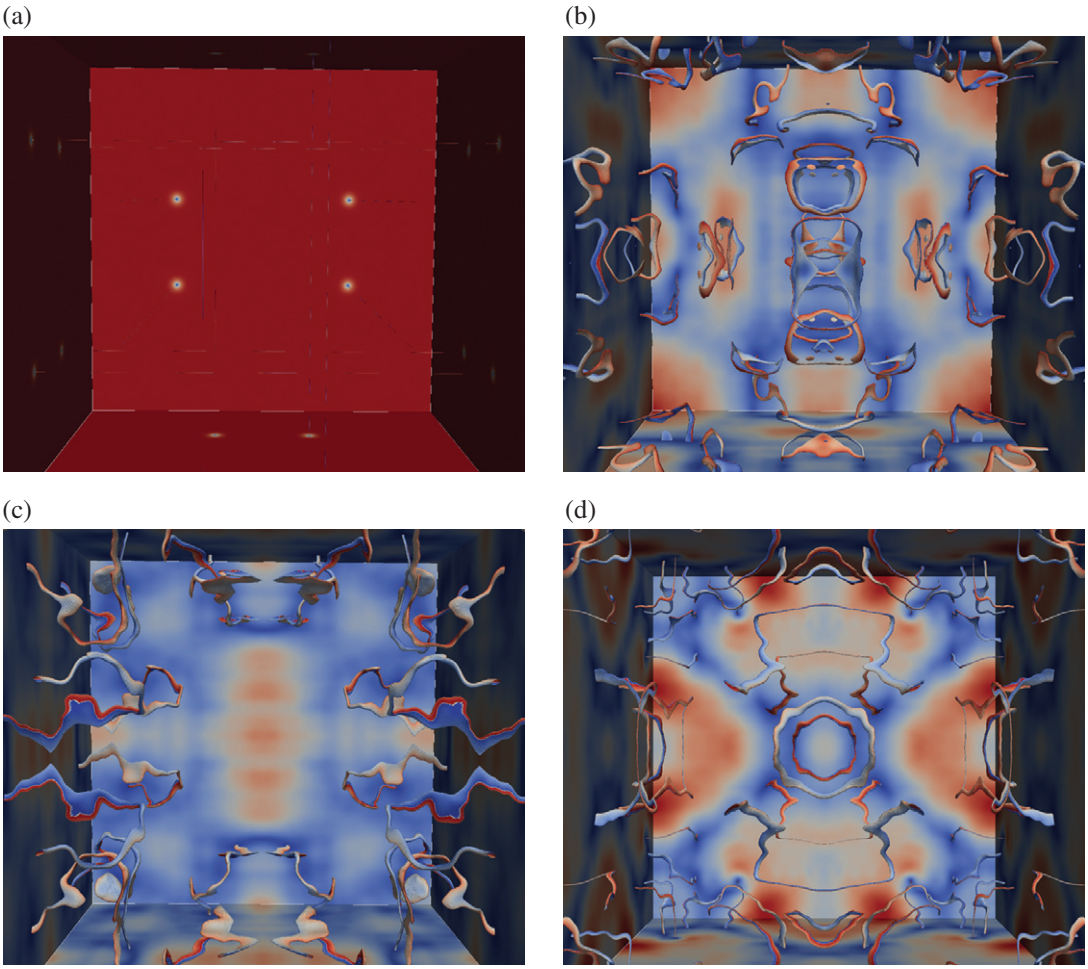


**Figure 7.** Isosurface plots of $|\varphi| / |\varphi|_{\max} = 1/64$ with phase information on the isosurfaces ($\phi = 0$ (blue) ; $\phi = 2\pi$ (red)), while on the walls we plot $|\phi|_{\text{walls}}$ values ranging from blue (low) to red (high). Higher initial internal energy $E_{\text{int}}(0) / E_{\text{kin}}(0) = 7.5 \times 10^{-2}$. (a) $t = 0$, (b) $t = 17\,400$, (c) $t = 57\,000$ and (d) $t = 79\,800$. The grid $L^3 = 1000^3$.

the detailed studies of the actual power law exponents due to the limited grid resolution. We have shown [21] that the Poincare recurrence time scales with the grid $L$ as $L^2$—i.e., as under diffusion ordering. For a very detailed study of the spectral exponents, see [21] where our unitary qubit lattice algorithms are run on a grid up to $3072^3$.

The vortex core isosurfaces for $E_{\text{int}}(0) / E_{\text{kin}}(0) = 7.5 \times 10^{-2}$ are shown in figure 7 and these should be compared to those with very low internal energy (figure 4). At these higher internal energies there are no vortex loop minimizations (as in figure 4(c)) or a semi-Poincare recurrence (figure 4(d)). One also sees considerable effects of compressibility on the walls with $|\varphi|$-values being blue for minima and red for maxima.

## 4. Skyrmions

Skyrme [35] started discussing topologically stable defects in a continuous field—objects that are now called skyrmions—which are localized in space with a quantized topological charge that can undergo interactions and form ordered phases and undergo phase transitions. Because of these particle-like properties they have been studied as baryion elementary particle theory [35], in liquid crystals [36], BECs [37], and quantum Hall effect [38, 39] and exhibit vortex lattice structure not unlike type II superconductors [40]. For our discussion

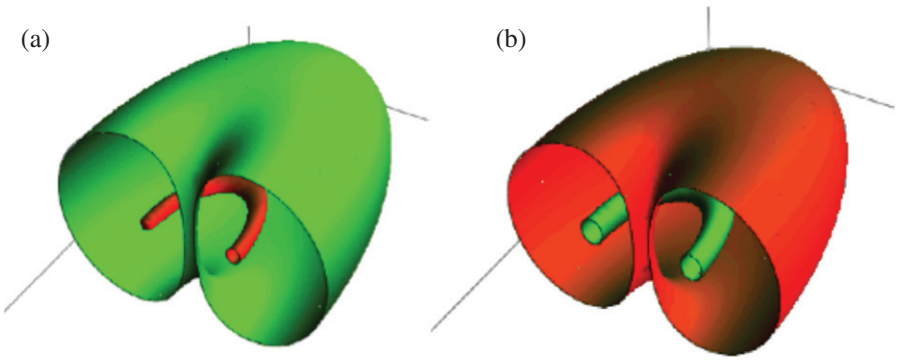


**Figure 8.** A vertical cut to display the isosurfaces of a skyrmion: (a) the vortex core consisting of a vortex ring (red) threaded by a somewhat linear vortex ($\varphi_-$ green) through the vortex ring $\varphi_-$ and which then encloses the vortex ring toroidally. $|\varphi_+|^2 = |\varphi_-|^2 = 0.04$ isosurface. (b) The corresponding isosurfaces for the asymptotic state of the spinor wave function: $|\varphi_+|^2 = |\varphi_-|^2 = 0.90$ isosurface.

of skyrmions, we consider a set of coupled BECs with a spinor wave function $\Phi$ satisfying

$$\mathrm{i}\frac{\partial \Phi}{\partial t} = -\nabla^2 \Phi + a\,(g\rho - 1)\,, \text{ with } \Phi = \begin{pmatrix} \varphi_+ \\ \varphi_- \end{pmatrix}, \quad \rho = |\varphi_+|^2 + |\varphi_-|^2\,. \tag{11}$$

The vortex core isosurfaces of this spinor wave function and the corresponding spatial far-field asymptotics of $|\Phi|$ are shown in figure 8.

The initial skyrmion wave function, axes centered at the origin, is given by

$$\Phi\,(\mathbf{x}) = \begin{pmatrix} \cos\left[\pi\,\tanh\,(kr) - \mathrm{i}\frac{z}{r}\sin\left[\pi\,\tanh\,(kr)\right]\right] \\ -\mathrm{i}\left[1 - \frac{z^2}{r^2}\right]^{1/2}\sin\left[\pi\,\tanh\,(kr)\right]\exp\,[\mathrm{i}\theta] \end{pmatrix}, \tag{12}$$

with $r = (x^2 + y^2 + z^2)^{1/2}$, $\theta = \tan^{-1}(y/x)$ and where $L^3$ is the simulation volume. The spinor wave function asymptotes to (relative to the origin)

$$\Phi_0 = \begin{pmatrix} \varphi_+ \\ \varphi_- \end{pmatrix}_0 = \begin{pmatrix} -1 \\ 0 \end{pmatrix}. \tag{13}$$

In our simulation we consider the expansion of a skyrmion in a simulation box of $1024^3$ and show the evolution of the skyrmion vortex core $|\Phi|$ (figure 9(a)). By $t = 150$ (figure 9(b)), the vortex ring for the component $|\varphi_+|$ thickens and descends and forms a capula structure by $t = 1000$ (figure 9(c)), while the vortex threading the vortex ring is expanding and starts to interact with the periodic boundaries just after $t = 2500$ (figure 9(d)). The outer surface of the topological defect for $|\varphi_-|$ rapidly deforms into a lattice structure with the topological defect for $|\varphi_+|$ forming capulas on many, but not all, of the lattice structure defects (figures 9(e) and (f)) of $|\varphi_-|$. The periodicity of the lattice structure varies throughout the run and we seem to find a somewhat random lattice of Skyrmion-like defects. Since the filling fraction of the vortex ring condensate $|\varphi_+|$ is too low to support quantum vortex rings around all the quantum vortex nodal lines of $|\varphi_-|$ in the lattice, the $|\varphi_+|$ condensate appears to randomly percolate throughout the lattice of the $|\varphi_-|$ condensate.

The energy spectra during the time evolution of the skyrmion are also quite interesting. At $t = 0$, for the $\varphi_-$ condensate, the kinetic energy and quantum energy spectra exhibit, for $k > 50$, the somewhat familiar $k^{-3}$ spectrum, while the internal energy spectrum rapidly decays for $k > 20$ (figure 10(a)). By $t = 1000$, there is a sharp increase in the very low wave number region of these spectra, followed by a subsequent drop for $k > 7$ (figure 10(b)). The spectral fit to the quantum energy spectrum for $75 \leqslant k \leqslant 300$ yields a $k^{-3.00}$ spectrum (dashed black line in figure 10(b)).

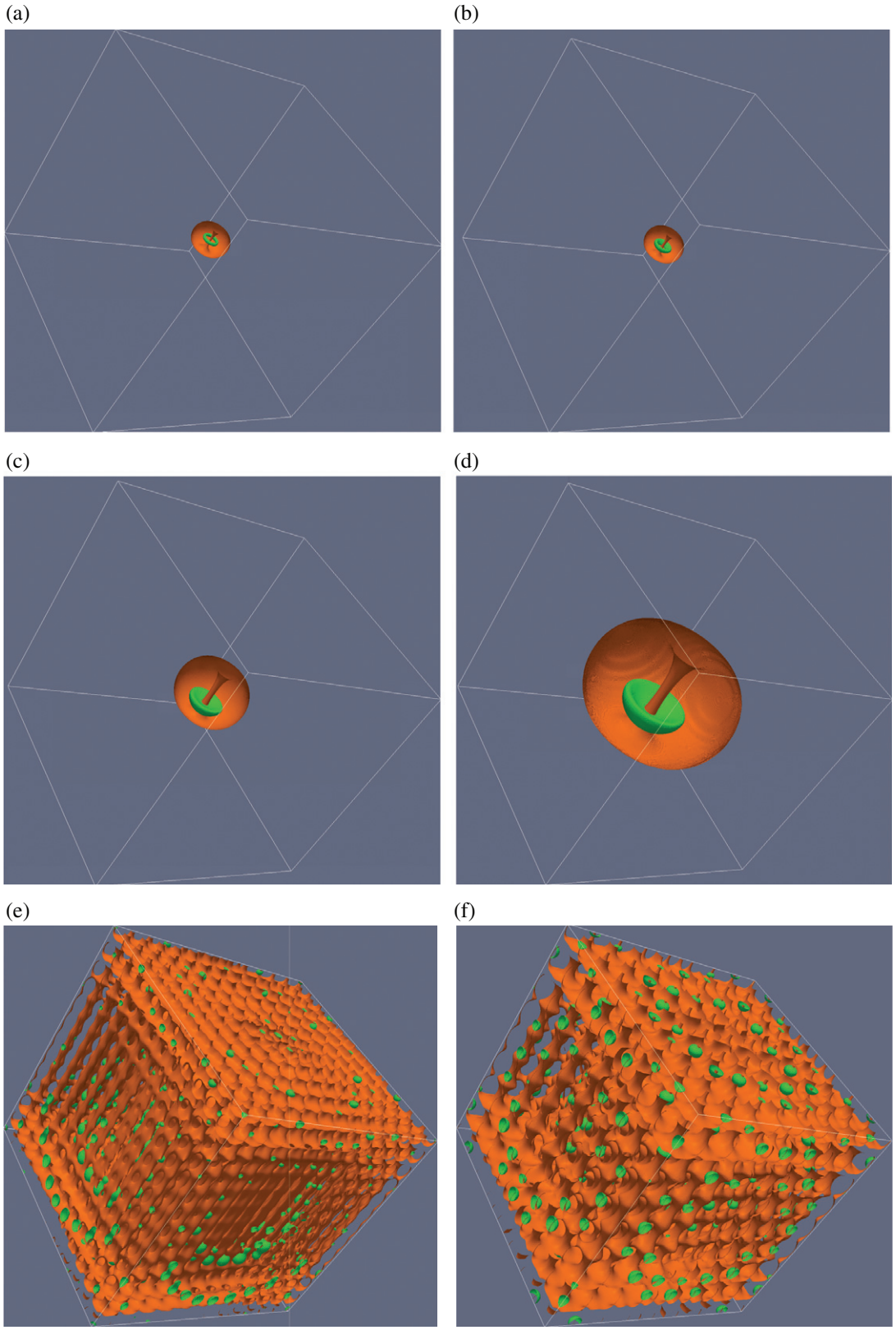


**Figure 9.** The evolution of the spinor quantum core of a skyrmion. The single skyrmion rapidly breaks into a lattice of percolating skyrmions. These isosurfaces are formed by culling the front to expose the innards. (a) $t = 0$, (b) $t = 150$, (c) $t = 1000$, (d) $t = 2500$, (e) $t = 7000$, (f) $t = 10\,500$, (g) $t = 17\,000$, (h) $t = 21\,000$, (i) $t = 22\,000$, (j) $t = 24\,000$, (k) $t = 28\,000$ and (l) $t = 29\,000$.

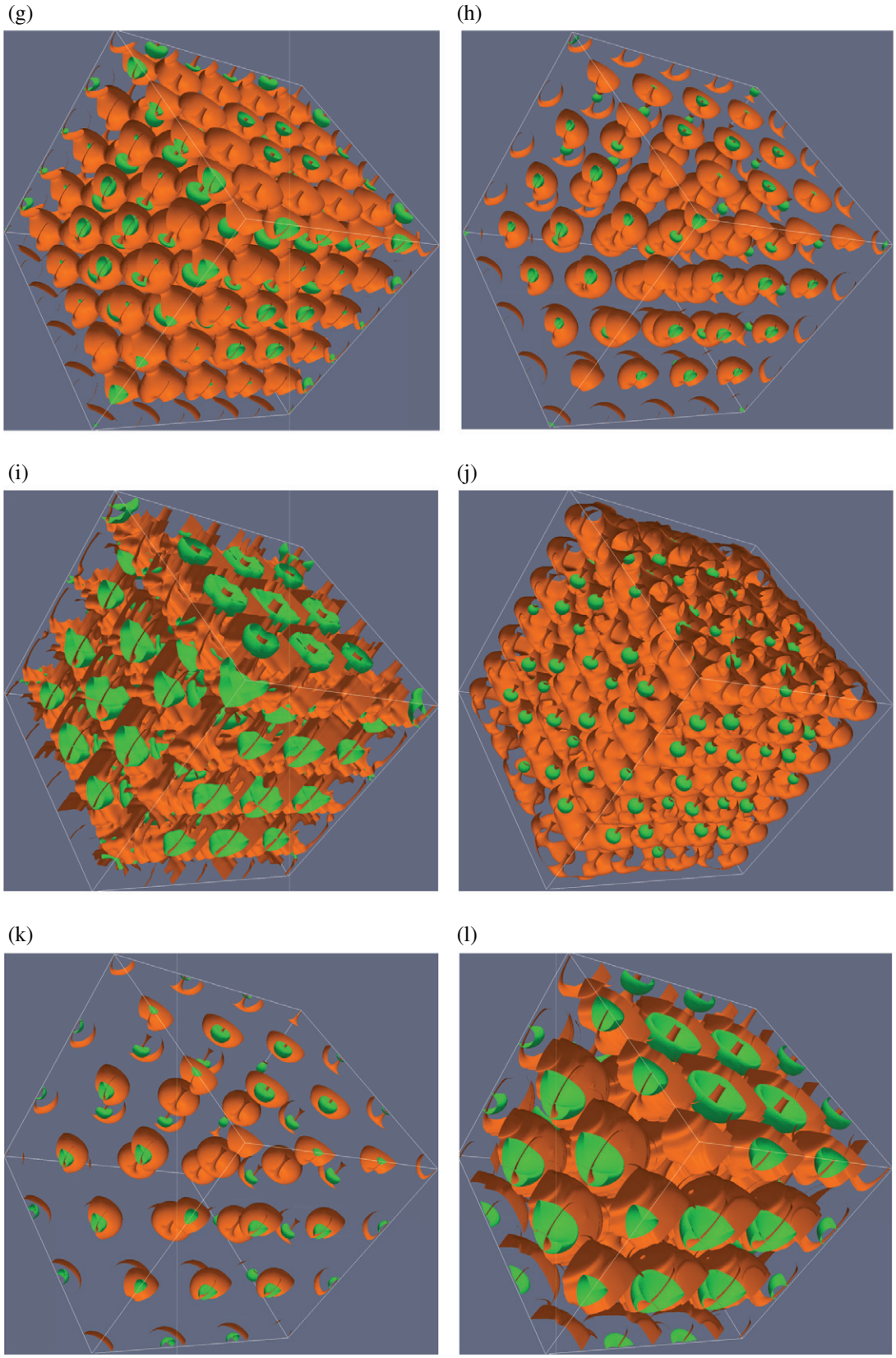


**Figure 9.** Continued.

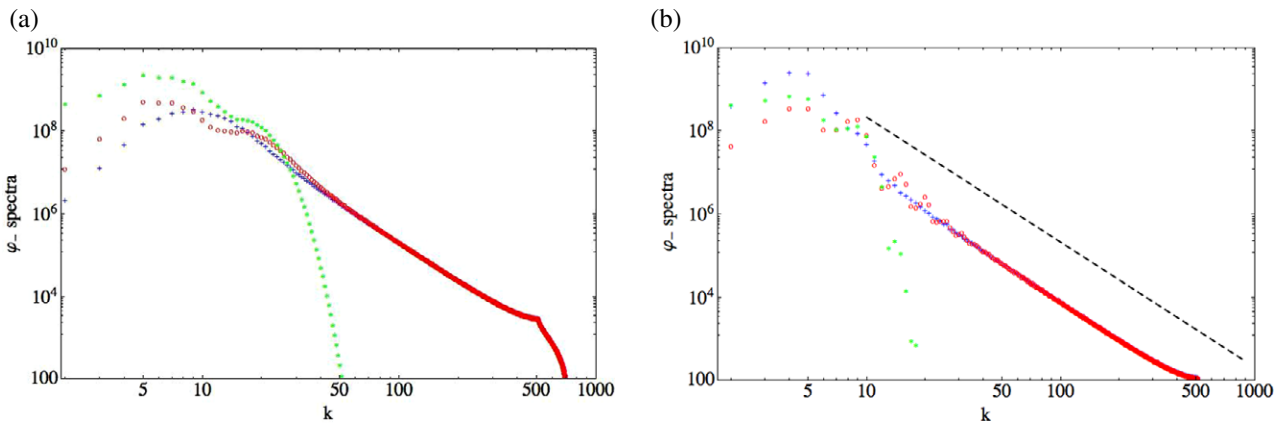


**Figure 10.** The kinetic (blue), quantum (red) and internal (green) kinetic energy spectra for the 'linear-toroidal' vortex core condensate $\varphi_-$, corresponding to the isosurface plots of figure 9. The dashed black line in (b) is for a $k^{-3}$ spectrum. (a) $t = 0$ and (b) $t = 1$ K.

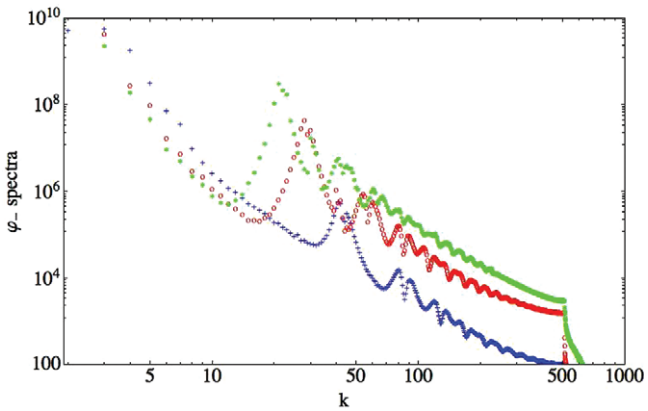


**Figure 11.** The time evolution of the kinetic energy spectrum at $t = 2000$ (blue), $t = 3000$ (red) and $t = 4000$ (green) for $\varphi_-$ condensate.

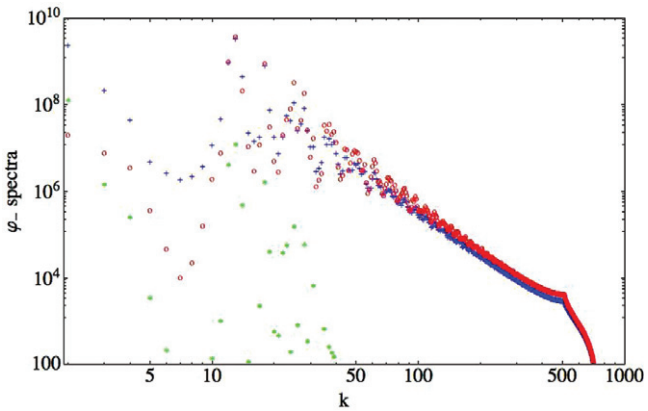


**Figure 12.** The kinetic (blue), quantum (red) and internal (green) energy spectra for $t = 7000$ for the $\varphi_-$ condensate.

Quite strong oscillations now occur in both the kinetic and the quantum energy spectra with higher peak magnitudes occurring at lower and lower $k$, see figure 11 (for $t = 2000$ (blue), $t = 3000$ (red) and $t = 4000$ (green)). The strength of these oscillations gradually decays (figure 12) and the spectra again exhibit the large-$k$ $k^{-3}$ spectrum.

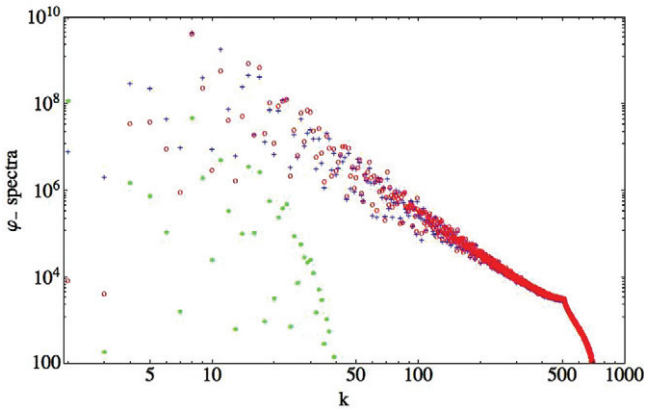


**Figure 13.** Noisy kinetic (blue) and quantum (red) energy spectra at $t = 24\,000$, with spectral exponent $k^{-\alpha}$, $\alpha = 0.33$ for condensate $\varphi_-$.

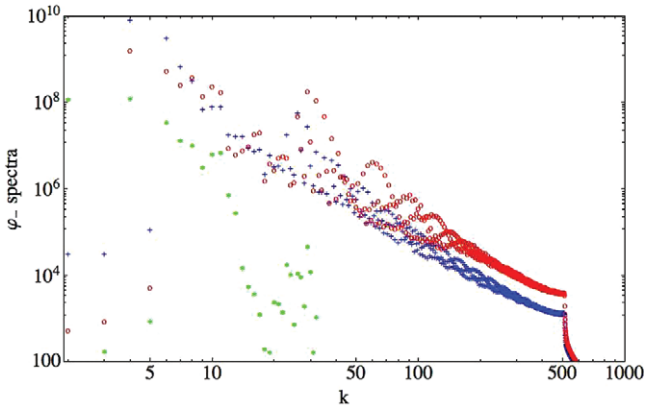


**Figure 14.** Rope-like oscillations in the kinetic (blue) and quantum (red) energy spectra for the linear-toroidal condensate $\varphi_-$ at $t = 27\,000$.

Typically, the spectra for the $\varphi_-$ condensate are similar to those in figure 12, but with the oscillations damped out. However at certain time intervals, in particular at $t = 14\,000$, $17\,000$, $20\,000$ and $24\,000$, the spectra become quite noisy (figure 13), while at times $t = 22\,000$, $27\,000$ and $29\,000$ there are quite strong rope-like structures (figure 14).

The spectra for the vortex ring condensate $\varphi_-$ behaves somewhat differently. Initially, the kinetic and quantum kinetic energies have a mild oscillation with the spectrum being predominantly $k^{-3}$ for large $k (k > 50)$ (figure 15). However, this $k^{-3}$ spectrum is rapidly destroyed and one sees a very steep non-power law decay for $t \geqslant 2000$ (figure 16).

During this evolution the internal energy spectrum increases for small $k (k < 5)$ and then the spectra are approximately unchanged for $2000 < t < 30\,000$, i.e., to the full run of this simulation on a $1024^3$ grid (figure 17). The total energy is conserved to within 0.01% throughout the run.

## 5. Conclusion

Since our unitary qubit algorithm respects the Hamiltonian structure of the GP equation, we can examine the parameter regimes that yield very short Poincare recursion times. Here we have made quantitative simulations examining the loss of this very short Poincare time when the internal energy of the BEC is increased. The spectrum is more complex than one would expect if one were dealing only with a totally isolated quantum vortex. In a totally isolated quantum vortex the compressible energy is exactly zero: all the energy is incompressible. However, in the BEC superfluid, compressibility effects play an essential role in permitting

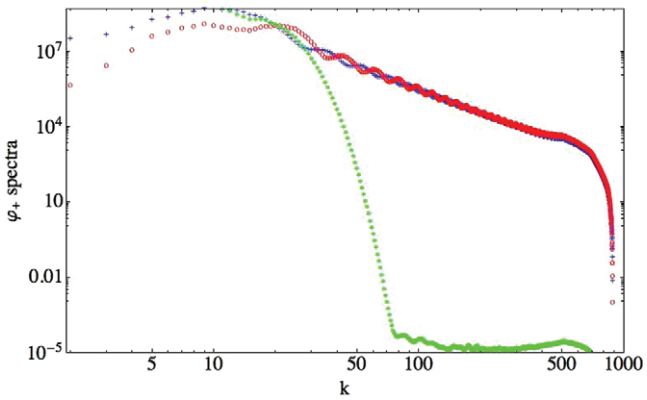


**Figure 15.** The initial kinetic (blue), quantum (red) and internal energy spectra for the vortex ring condensate $\varphi_-$.

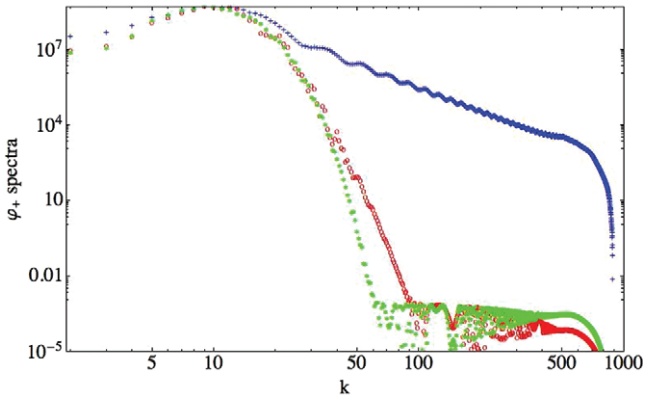


**Figure 16.** The development of the kinetic energy spectrum: $t = 0$ (blue), $t = 1000$ (red) and $t = 2000$ (green) for the condensate $\varphi_-$.

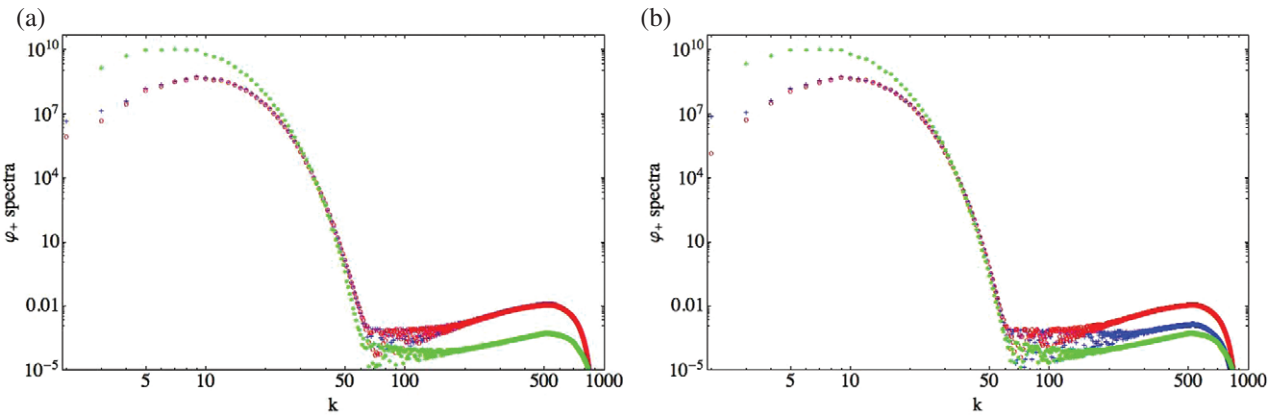


**Figure 17.** The kinetic (blue), quantum (red) and internal (green) energy spectra for (a) $t = 14\,000$ and (b) $t = 27\,000$. The spectra are basically invariant for $t > 2000$.

vortex reconnection. Moreover, we find that typically the compressible kinetic energy spectrum is greater than the incompressible kinetic energy spectrum for wave numbers $k > 20$. The incompressible kinetic energy typically exhibits only a $k^{-3}$ spectrum for wave numbers $k > 10$. However, the compressible spectrum and the quantum energy spectrum typically exhibit three spectral regions—but the interpretation of these spectral regions and whether they are even cascades is still an open question. It is very interesting to note that in classical

compressible fluid turbulence simulation models in which subgrid closures are necessarily employed because of grid resolution questions, the total subgrid kinetic energy spectrum is forced to yield the Kolmogorov $k^{-5/3}$ spectrum [34]. In our GP simulations [21], we actually solve for the total kinetic energy spectrum and find that it does yield a $k^{-5/3}$ spectrum for small $k$, but the incompressible energy spectrum remains $k^{-3}$. However, it is not clear whether this corresponds to the classical Kolmogorov energy spectrum (as determined from dimensional analysis for *incompressible* flows). The typical picture of the blending of quantum turbulence to classical turbulence [24–27] is that the quantized vortices are embedded within the 'largest' vortices of figure 1 and these bundled quantum vortices undergo the cascade. The belief is that the bundled quantum vortices are no longer quantized in the mean. No quantum simulations of the GP equation have explored this regime as yet and it seems a doubtful picture in light of the important role played by compressibility in the quantum turbulent flow. It is felt that nonlocal effects may be more important in quantum turbulence.

We have extended our unitary qubit algorithm for the scalar GP equation to handle multi-component BECs and, in particular, considered the evolution of an unstable skyrmion in a cubical box under periodic boundary conditions. The skyrmion under consideration had two vortex cores interlinked: one vortex core for the first condensate was a ring vortex threaded through its axis by a linear vortex core of the second condensate, which then toroidally enclosed the ring vortex of the first condensate. The toroidal surface of the second condensate rapidly breaks up into a lattice of such vortices. Since the density of the vortex ring first condensate is too low to populate all the quantum vortex nodal lines formed from the second condensate, we find that the multi-skyrmions formed have the vortex ring randomly percolating through the lattice. Moreover, there are what look like a breathing mode of the nodal vortex core with its toroidal closure and times when the skyrmions become isolated from each other. These dynamics are not heavily imprinted on the energy spectra.

Finally, we comment on the scaling of the physics at the mesoscopic level. Standardly, for three-dimensional lattice algorithms the physics would scale cubically with grid size: that is, if the physics in a lattice simulation on a grid $L_1$ occurred at time $t_2 = t_1\,(L_2/L_1)^2$, then on a grid $L_2$ the same physics will occur at time $t_2 = t_1\,(L_2/L_1)^3$. However, to recover the GP equation, we must have diffusion ordering (see the appendix): i.e. $t_2 = t_1\,(L_2/L_1)^2$. In the actual qubit numerical algorithm the only way to enforce the diffusion ordering is to restrict our simulations to parameter regimes in which the diffusion ordering is automatically obeyed. If one runs simulations outside this region, then at the macro level we will not be solving the GP equation itself.


## Acknowledgments

This work was supported by the AFOSR and the DoE. The computations were mainly performed at DoD HPCMP sites and some computations at the NERSC. The authors are grateful to Sean Ziegeler for the isosurface graphics routines, and Bo Zhang for discussions.


## Appendix. The unitary qubit lattice algorithm [3–10, 21, 22]

We will briefly outline the unitary qubit lattice algorithm for the scalar GP equation (3) and then discuss the extensions required in the algorithm to solve the coupled BECs (11). Instead of solving (3) directly we move to the mesoscopic level and introduce qubits on a spatial lattice whose moments will lead to the BEC ground state wave function $\varphi$. Since we will be using quantum entanglement and phase coherence at the mesoscopic level, we require at least two qubits per grid point. However, two qubits will be all that is required to recover the scalar GP equation (3), making the algorithm very light on processor memory and so permit large grid simulations to be performed with relatively few qubits. For example, production runs have been performed on grids of $5760^3$ using just under 12 000 cores.

Since we are using two qubits per lattice site, there are $2^2$ states. To recover the scalar wave function we need, consider the complex amplitudes of two of these states: $\alpha\,(\mathbf{x}, t)$ , $\beta\,(\mathbf{x}, t)$ and the time evolution of the vector

$$\psi\,(\mathbf{x}, t) = \begin{pmatrix} \alpha\,(\mathbf{x}, t) \\ \beta\,(\mathbf{x}, t) \end{pmatrix}. \tag{A.1}$$

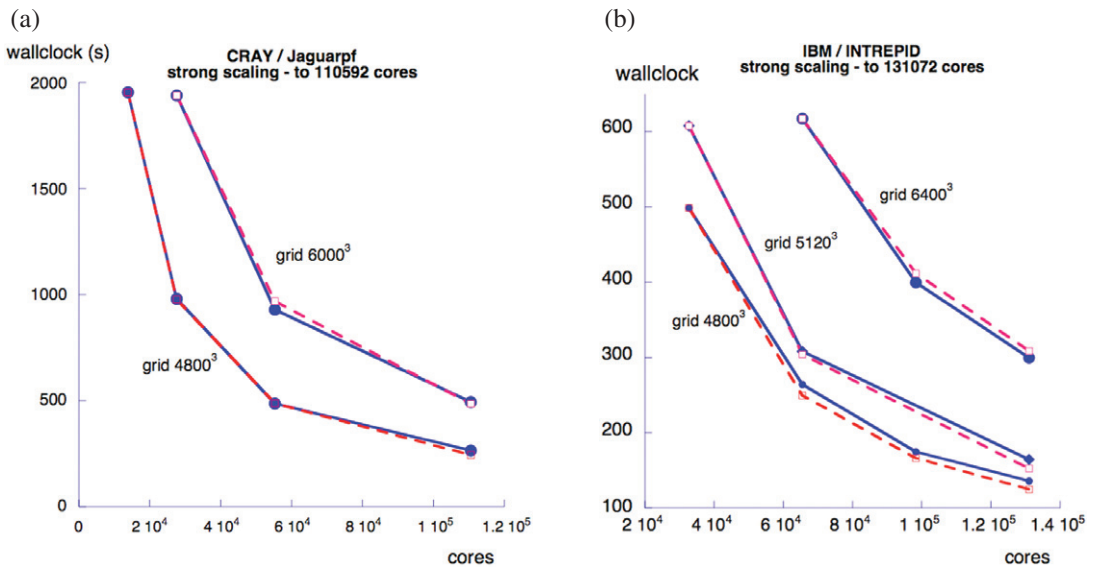


**Figure A.1.** The strong scaling of the unitary qubit codes on Jaguarpf (CRAY XT5 at Oak Ridge National Laboratory) and Intrepid (IBM BlueGene at Argonne National Laboratory). Ideal scaling is shown in dashed red (that is, on doubling the cores the wall clock is reduced by a factor of two). The strong scaling is up to 110 592 cores on Jaguarpf and 131 072 cores on Intrepid and the unitary code scaling is shown in blue.

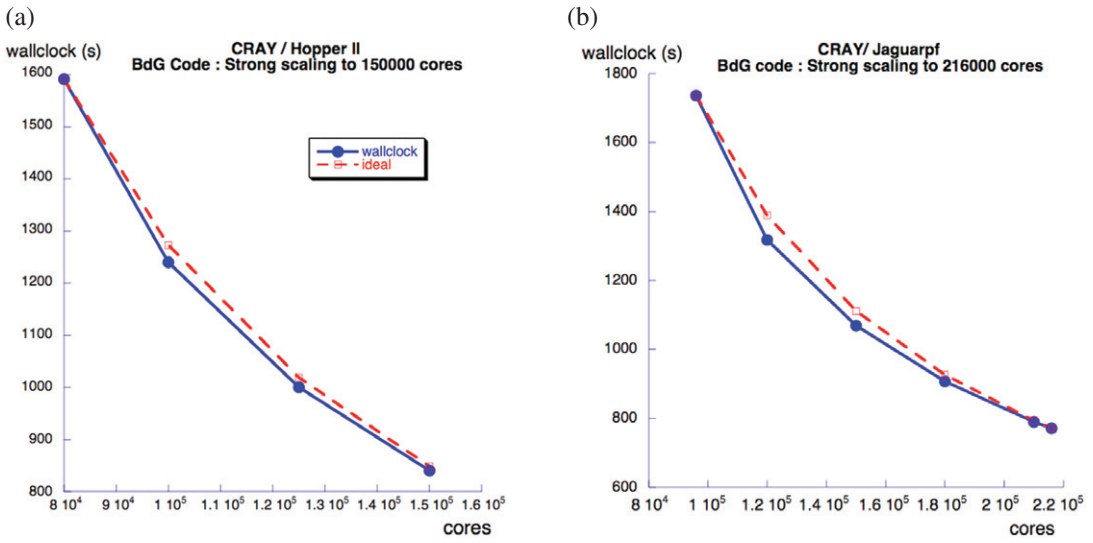


**Figure A.2.** The strong scaling of our coupled BEC unitary qubit codes on Hopper (CRAY XE6 at NERSC) and on Jaguarpf (CRAY XT5 at ORNL). Ideal scaling is shown in dashed red (that is, on doubling the cores the wall clock is reduced by a factor of two). The strong scaling is up to 150 000 cores on Jaguarpf and 216 000 cores on Intrepid and the unitary code scaling is shown in blue.

The unitary time evolution of this vector is achieved by a combination of the following three unitary operations: (i) a unitary collision operator $C$ that locally entangles these amplitudes; (ii) a unitary streaming operator $S$ that shifts just one of these amplitudes to the neighboring lattice site and eventually an exponential phase operator that incorporates the nonlinear $|\varphi|^2$ term into the GP equation. To recover the $\nabla^2$ operator, one needs to use the $2 \times 2$ unitary collision matrix

$$C = \frac{1}{2}\begin{pmatrix} 1-\mathrm{i} & 1+\mathrm{i} \\ 1+\mathrm{i} & 1-\mathrm{i} \end{pmatrix} \text{ with } C^2\begin{pmatrix}\alpha\\ \beta\end{pmatrix} = \begin{pmatrix}\beta\\ \alpha\end{pmatrix}, C^4 = I. \tag{A.2}$$

**Table A.1.** Weak scaling on Jaguarpf (CRAY XT5).

| Grid | Cores | Wallclock (s) |
|---|---|---|
| $600^3$ | 216 | 261.0 |
| $1200^3$ | 1 728 | 261.8 |
| $2400^3$ | 13 824 | 263.9 |
| $3600^3$ | 46 656 | 268.4 |

**Table A.2.** Weak Scaling on Hopper (CRAY XE6).

| Grid | Cores | Wallclock (s) |
|---|---|---|
| $600^3$ | 216 | 209.2 |
| $1200^3$ | 1 728 | 212.7 |
| $2400^3$ | 13 824 | 212.1 |
| $3600^3$ | 46 656 | 212.7 |
| $4000^3$ | 64 000 | 213.3 |
| $4800^3$ | 110 592 | 214.0 |

Because of (A.2), $C$ is usually called the square-root-of-swap operator. The streaming shift operator

$$S_{\Delta x,1}\begin{pmatrix}\alpha\,(\mathbf{x})\\ \beta\,(\mathbf{x})\end{pmatrix}=\begin{pmatrix}\alpha\,(\mathbf{x}+\Delta\mathbf{x})\\ \beta\end{pmatrix},\quad S_{-\Delta x,2}\begin{pmatrix}\alpha\,(\mathbf{x})\\ \beta\,(\mathbf{x})\end{pmatrix}=\begin{pmatrix}\alpha\,(\mathbf{x})\\ \beta\,(\mathbf{x}-\Delta\mathbf{x})\end{pmatrix}, \tag{A.3}$$

where the subscript '1' refers to shifts on the amplitude $\alpha$ and '2' to the amplitude $\beta$. The unitary operators $C$ and $S$ do not commute: $[C, S] \neq 0$. We consider the following sequence of interleaved operators, with $\gamma = 1$ or 2:

$$J_{z\gamma} = S_{-\Delta z,\gamma} C S_{\Delta z,\gamma} C, \tag{A.4}$$

with the time evolutionary operator incorporating an exponential phase factor $\Omega$ to be specified later,

$$U_\gamma[\Omega] = J_{x\gamma}^2 J_{y\gamma}^2 J_{z\gamma}^2 \exp\left[-\mathrm{i}\quad \varepsilon^2\quad \Omega\right], \varepsilon \ll 1, \tag{A.5}$$

and $\varepsilon$ a small perturbative parameter. Under this evolutionary operator

$$\psi\,(\mathbf{x}, t+\Delta t) = U_\gamma\,[\Omega]\,\psi\,(\mathbf{x}, t)\,,$$

one can show under perturbation theory that, where $I$ is the identity matrix and $\Delta x = O(\varepsilon)$,

$$\psi\,(\mathbf{x}, t+\Delta t) = \psi\,(\mathbf{x}, t) - \mathrm{i}\varepsilon^2\left[-\frac{1}{2}\begin{pmatrix}0 & 1\\ 1 & 0\end{pmatrix}\nabla^2 + \Omega I\right]\psi\,(\mathbf{x}, t) + \frac{(-1)^\gamma}{4}\varepsilon^3\begin{pmatrix}1 & -\mathrm{i}\\ \mathrm{i} & -1\end{pmatrix}\nabla^2\psi\,(\mathbf{x}, t) + O(\varepsilon^4). \tag{A.6}$$

Since the $O(\varepsilon^3)$-term in (A.6) alternates with sign depending on whether $\gamma = 1$ or 2, it can be eliminated by symmetrizing the evolution operator

$$U[\Omega] = U_2\left[\frac{\Omega}{2}\right]U_1\left[\frac{\Omega}{2}\right], \psi(\mathbf{x}, t+\Delta t) = U[\Omega]\psi(\mathbf{x}, t). \tag{A.7}$$

Moreover, under diffusion ordering: $\Delta x = O(\varepsilon)$, $\Delta t = O(\varepsilon^2)$, the vector qubit amplitude evolution equation becomes

$$\mathrm{i}\frac{\partial}{\partial}\psi(\mathbf{x}, t) = \left[-\frac{1}{2}\begin{pmatrix}0 & 1\\ 1 & 0\end{pmatrix}\nabla^2 + \Omega\right]\psi(\mathbf{x}, t) + O(\varepsilon^2). \tag{A.8}$$

On rescaling the gradient operator $\nabla \to a^{-1}\nabla$ and contracting the vector $\psi$ into the scalar $\varphi$

$$(1\quad 1)^\psi = (1\quad 1)\begin{pmatrix}\alpha\\ \beta\end{pmatrix} = \alpha + \beta \equiv \varphi, \tag{A.9}$$

one recovers the desired GP equation (3) under the choice $\Omega \equiv g\,|\varphi|^2 - 1$,

$$\mathrm{i}\frac{\partial \varphi}{\partial t} = -\nabla^2\varphi + a\left(g\,|\varphi|^2 - 1\right)\varphi. \tag{A.10}$$

The extension of our qubit algorithm to the spinor BEC (11) is immediate, simply requiring four qubits per grid node: two qubits for $\Omega_\pm$ and two qubits for $\varphi_-$. For a more general coupling between the two BECs, one need simply to introduce two different exponential phasing factors $\Omega_\pm$.

The beauty of the qubit unitary algorithm is that its major operations are purely local collisional entanglement and then that entangled information is appropriately streamed to the neighboring lattice site. This permits near-ideal parallelization on current supercomputers and also permits direct application to quantum computers once they become available due to the unitary nature of the algorithm. Moreover, it fully respects the Hamiltonian nature of the GP (3) and thus permits the investigation of Poincare recurrence.

In figures A.1 and A.2, we show the strong scaling results of our unitary codes. In strong scaling, one fixes the lattice grid and sees how the code's wallclock time decreases in proportion to the increase in the number of cores.

One can thus see that the unitary codes are even scaling superlinearly, as seen in figure A.2 with the blue curve lying below the ideal scaling (shown in red).

The weak scaling of the unitary codes is also excellent, as seen in tables A.1 and A.2 In weak scaling, one tests the wall clock time as the work done by each processor is kept constant as one increases the number of cores (that is, if one doubles the grid in each dimension, then one would increase the number of cores by a factor of $2^3$).

## References


[1] Pope S 1990 *Turbulent Flows* (Cambridge: Cambridge University Press)
Biskamp D 2003 *Magnetohydrodynamic Turbulence* (Cambridge: Cambridge University Press)
Tusbota M 2008 *J. Phys. Soc. Japan* **77** 111006
Pethick C and Smith H 2009 *Bose–Einstein Condensation in Dilute Gases* (Cambridge: Cambridge University Press)
[2] Kasamatsu K, Tsubota M and Ueda M 2005 *J. Mod. Phys.* B **19** 1835–902
[3] Yepez J 1998 *Int. J. Mod. Phys.* C **9** 1587
[4] Yepez J 2001 *Phys. Rev.* E **63** 046702
[5] Yepez J and Boghosian B 2002 *Comput. Phys. Commun.* **146** 280
[6] Vahala G, Vahala L and Yepez J 2003 *Phys. Lett.* A **310** 187–96
[7] Vahala G, Vahala L and Yepez J 2004 *Phil. Trans. R. Soc.* A **362** 215
[8] Vahala G, Vahala L and Yepez J 2006 *Physica* A **362** 215
[9] Vahala G, Soe M, Zhang B, Yepez J, Vahala L, Carter J and Ziegeler S 2011 *Int. Conf. SC-11* http://sc11.supercomputing.org/?pg=papers.hmtl
[10] Yepez J, Vahala G, Vahala L and Soe M 2009 *Phys. Rev. Lett.* **103** 084501
Yepez J, Vahala G, Vahala L and Soe M 2009 *Phys. Rev. Lett.* **110** 129402
[11] Nore C, Abid M and Brachet M E 1997 *Phys. Fluids* **9** 2644–69
[12] Kobayashi M and Tsubota M 2007 *Phys. Rev.* A **76** 045603
[13] Barenghi C F 2008 *Physica* D **237** 2195
[14] Vinen W F and Niemela J J 2002 *J. Low Temp. Phys.* **128** 167
[15] Vinen W F 2005 *J. Phys. Condens. Matter* **17** S3231–8
[16] Donnelly R J 1991 *Quantized Vortices in Helium II* (Cambridge: Cambridge University Press)
[17] Gross E P 1963 *J. Math. Phys.* **4** 195
Pitaevskii L P 1961 *Sov. Phys.—JETP* **13** 451
[18] Sulem C and Sulem P L 1999 *The Nonlinear Schrodinger Equation* (Berlin: Springer)
Kivshar Y S and Agrawal G 2003 *Optical Solitons* (New York: Academic)
[19] Afraimovich V, Ugalde E and Urias J 2006 *Fractal Dimensions for Poincare Recurrence* (Amsterdam: Elsevier)
[20] Zaslavsky G 2005 *Hamiltonian Chaos and Fractional Dynamics* (Oxford: Oxford University Press)
[21] Vahala G, Yepez J, Vahala L, Soe M, Zhang B and Ziegeler S 2011 *Phys. Rev.* E **84** 046713
[22] Zhang B, Vahala G, Vahala L and Soe M 2011 *Phys. Rev.* E **84** 046701

[23] Clements G M 1986 *Topics in Skyrmion Physics* (Ithaca, NY: Cornell University Press)
Manton N and Sutcliffe P 2004 *Topological Solitons* (Cambridge: Cambridge University Press)
[24] Barenghi C F, Samuels D C, Bauer G H and Donnelly R J 1997 *Phys. Fluids* **9** 2631–43
[25] Vinen W F 2000 *Phys. Rev.* B **61** 1410–20
[26] Walmsley P M, Golov A I, Hall H E, Levchenko A A and Vinen W F 2007 *Phys. Rev. Lett.* **99** 265302
[27] Paoletti M S and Lathrop D P 2011 *Ann. Rev. Condens. Matter Phys.* **2** 213–34
[28] Berloff N 2004 *J. Phys. A: Math. Gen.* **37** 1617
[29] Feynman R P 1955 *Progress in Low Temperature Physics* vol 1 (Amsterdam: North-Holland) pp 17–53
[30] Koplik J and Levine K 1993 *Phys. Rev. Lett.* **71** 1375
[31] Bewley G P, Paoletti M S, Sreenivasan K R and Lathrop D P 2008 *Proc. Natl Acad. Sci. USA* **105** 13707
[32] Paoletti M S, Fisher M E and Lathrop D P 2010 *Physica* D **239** 1367–77
[33] Steckline V S 1983 *Am. J. Phys.* **51** 894–7
[34] Genin F and Menon S 2010 *J. Turbul.* **1** 1
[35] Skryme T H 1961 *Proc. R. Soc. Lond.* A **260** 127–38
[36] Wright D C and Mermin N D 1989 *Rev. Mod. Phys.* **61** 385–432
[37] Al'Khawaha U and Stoof H T 2001 *Nature* **411** 918–20
[38] Sondhi S L, Karlhede A, Kivelson S A and Rezayi E H 1993 *Phys. Rev.* B **47** 16419
[39] Brey L, Fertig A H, Cote R and MacDonald A H 1995 *Phys. Rev. Lett.* **75** 2562–5
[40] Abrikosov A A 2004 *Rev. Mod. Phys.* **76** 975